Chapter 17
THz Devices Based on Carbon Nanomaterials

Mircea Dragoman and Daniela Dragoman

Abstract In this chapter we present a review the terahertz devices based on carbon nanomaterials such as graphene and carbon nanotubes. First, the graphene and carbon nanotube physical properties at high frequencies are described. Then, antennas at terahertz frequencies based on graphene, the generation and detection of terahertz electromagnetic waves are analyzed and different devices and circuits are discussed.

17.1 Introduction

Since the early 90s the research regarding post-CMOS electronics, i.e. the most advanced electronic devices to date, has been enhanced by a new class of materials based on organized aggregation of carbon atoms. Carbon nanotubes (CNTs), discovered in 1991 [1], have been considered as key nanomaterials for the post-CMOS era due to their extremely promising electrical and mechanical properties.

In 2004, the isolation of single atom-sheet matter consisting of carbon atoms, known as graphene, triggered one of the most studied subjects by the physicist' community [2]. Nowadays, graphene is becoming a central subject in electronic engineering [3], as well as many applied areas of physics, such as photonics [4]. THz devices based on CNTs or graphene are at the border between electronics and photonics.

Graphene is the first material in a large class of two-dimensional (2D) materials formed from a single atomic sheet. The exploration of physical properties of graphene

M. Dragoman (✉)
National Institute for Research and Development in Microtechnology, 077190 Bucharest-Voluntari, Romania
e-mail: mircea.dragoman@imt.ro

D. Dragoman
University of Bucharest, 077125 Bucharest-Magurele, Romania

D. Dragoman
Academy of Romanian Scientists, Spalaiul Independentei 54, 050094 Bucharest, Romania

I. Tiginyanu et al. (eds.), *Nanostructures and Thin Films for Multifunctional Applications*, NanoScience and Technology,
DOI 10.1007/978-3-319-30198-3_17

has started by isolating graphene flakes followed by their subsequent transfer on a doped Si/SiO_2 substrate [5]. The transfer method of graphene, grown by the chemical vapor deposition method, on various substrates is the key concept for batch production of graphene monolayers at 4-inch and 6-inch wafer scale, 12-inch wafers being expected only in the next few years [6]. In fact, the discovery of graphene was motivated by the search of a metallic field-effect transistor (FET), which would be much less influenced by electromagnetic radiation than a semiconductor transistor [7].

Searching for the electric field effect (EFE) in common metals was unsuccessful due to the very large number of carriers which needed to be controlled by an electric field. Therefore, other experiments were performed in semimetals such as Bi [8], antimony and graphite, which have a much smaller carrier density compared to a metal [7]. This search was at the origin of the breakthrough that led to the discovery of graphene from graphite. An in-depth review of EFE in various materials is found in [9]. The quest for a metallic transistor was successful in 2012 [10] when an ultrathin Ni film with a thickness of 1–2 nm showed a graphene transistor-like behavior. Further, metallic switches and logic gates were developed based on thin films of 2H-$TaSe_2$, which is a semimetal without bandgap [11]. The EFE is now investigated in other 2D materials, such as black phosphorus [12]. The most advanced device derived from the EFE is the CMOS FET, developed in Si technology, due to its impressive integration capability and reduced consumption. For example, 5.4 billion transistors were recently integrated in a neuromorphic Si chip [13]. The first high-frequency integrated circuit based on graphene—a microwave receiver—has only three transistors [14]. The CNT and graphene are investigated in-depth from the manufacturing point of view and from the experimental and theoretical perspective, in order to achieve large scale production with high reproducibility, controlled chirality, and material purity. A recent review about CNT growth and its ultimate performances and applications is found in [15]. The physical properties of these new nanomaterials determines the macroscopic enhanced or novel electrical behavior of many devices applied in electronics, harvesting, biosensing and photonics [16, 17]. The main physical properties useful for THz electronics of CNTs and graphene are summarized in Tables 17.1 and 17.2.

Carbon electronics is more advanced than graphene electronics—see the review paper [18]. The most prominent success of CNT electronics is a computer having thousands of integrated CNT FET transistors [19]. The CNT computer processor is

Table 17.1 Graphene properties

Parameter	Room temperature values
Mean free path (ballistic transport)	400 nm, even 1 μm for graphene deposited on hexagonal BN
Mobility	40000 cm^2/Vs (intrinsic), but could attain 100000 cm^2/Vs in suspended graphene or in graphene deposited on hexagonal BN
Effective mass of carriers	0 near the Dirac point
Thermal conductivity	5000 W/mK, better than in many metals

Table 17.2 Carbon nanotube properties

Parameter	Room temperature values	Observations
Current density	$>10^9$ A/cm^2	1000 times larger than in copper
Mobility	10000–50000 cm^{2}V^{-1}s^{-1}	Lower than in graphene
Mean free path (ballistic transport)	300–700 nm in semiconducting CNTs 1000–3000 nm in metallic CNTs	At least three times larger than in the best semiconducting heterostructures

comparable in capabilities to the Intel 4004, which was the first programmable microprocessor and thus the ancestor of microprocessors found today in any computer. Such CNT-based computers could be more energy-efficient than silicon-based computers. In contrast to CNTs, which have a clear perspective for development in digital engineering, graphene electronics is oriented toward high-frequency electronics, since the lack of bandgap in graphene is a serious obstacle towards digital applications.

From all parameters in Tables 17.1 and 17.2, the most important property of graphene and CNTs is the long ballistic transport distances at room temperature. For comparison, the mean free path at room temperature is of only 150 nm in InAs nanowires [20], while the highest mean free path reported in semiconductors at room temperature is found in InSb/AlInSb quantum wells, being of 550 nm [21] at a current density of 10^6 A/cm^2, while in CNTs and graphene at similar or longer mean free paths the current density is higher with two or three orders of magnitudes. This implies that charge carriers in CNTs and graphene travel coherently over hundreds of nanometers at room temperature, without any collision, which explains the high mobilities of these materials.

These facts have important implications for high-frequency devices. More precisely, (i) the large mean free paths allows the fabrication of ballistic high-frequency devices based on CNTs and graphene at room temperature since the minimum features of existing nanolithography such e-beam is below 10 nm, (ii) the cutoff frequency of CNT and graphene ballistic devices are in the THz range since the cutoff frequency $\propto v_F/L$, where L is the mean free path at room temperature and v_F is the Fermi velocity. For example in metallic CNTs the Fermi velocity is 9.3×10^5 m/s while in graphene monolayer this parameter takes a value of about 10^6 m/s.

The knowledge of the electronic band structure of graphene is necessary to understand other properties of CNTs and graphene for THz electronics. The honeycomb structure of carbon atoms, which constitute a graphene layer and can be understood as a superposition of two triangular lattices, is displayed in Fig. 17.1a. The distance between carbon atoms, i.e. the carbon bond length, is of $a = 0.14$ nm and the unit cell is spanned by the two vectors $\boldsymbol{a}_1$ and $\boldsymbol{a}_2$. The reciprocal lattice has also a honeycomb shape. The first Brillouin zone, which is a hexagon with a side length of $4\pi/3\sqrt{3}a$, is displayed in Fig. 17.1b. The non-equivalent points K and K',

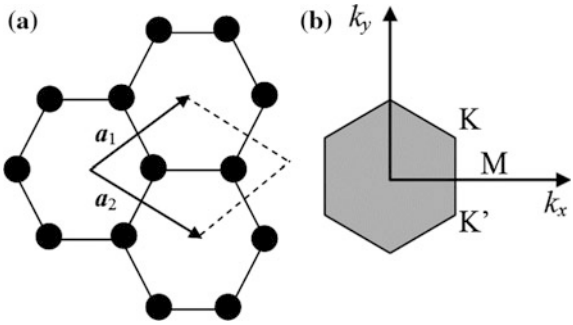

Fig. 17.1 **a** Graphene honeycomb lattice structure and **b** the first Brillouin zone in the reciprocal lattice

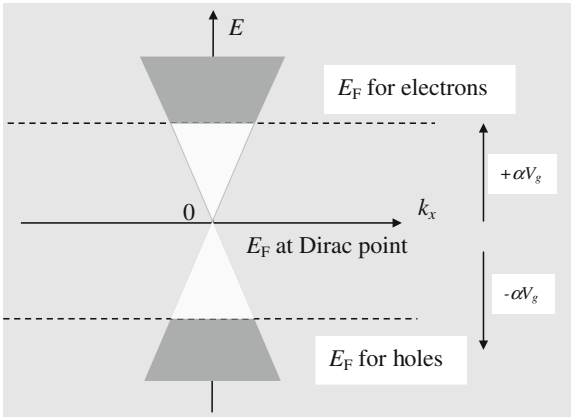

Fig. 17.2 Graphene dispersion relation

called Dirac points, are the most important points in the reciprocal lattice, because the dispersion relation of graphene, given by [22]

$$E(\boldsymbol{k}) = \pm t\sqrt{3 + 2\cos(\sqrt{3}k_y a) + 4\cos(\sqrt{3}k_y a/2)\cos(3k_x a/2)} \tag{17.1}$$

reduces to the linear relation

$$E = \pm\hbar|\boldsymbol{k}|v_F \tag{17.2}$$

near the K and K' points, where $\boldsymbol{k} = \boldsymbol{i}k_x + \boldsymbol{j}k_y$ is the wavenumber measured from K and K', and the positive (negative) sign is assigned to electron (hole) states. The dispersion relation (2) consists of two cones represented in Fig. 17.2.

From Fig. 17.2 we observe that graphene is a semiconductor with no energy gap, because the valence and conduction bands touch at Dirac points. The linear dispersion relation in graphene is not encountered in nature except for photons propagating in a homogeneous medium. Therefore, the graphene dispersion relation is photon-like and graphene can be modeled as a 2D gas of massless carriers. More precisely, graphene is similar to a slow-wave structure, in which the charge carriers

propagate with a velocity $v_F \cong c/300$, which is two orders of magnitude smaller than light velocity of vacuum c. In striking contrast with a semiconductor, the electrons and holes in graphene have identical physical properties, and their selection is done by a gate voltage that shifts the Fermi energy level E_F above and below the Dirac point, where $E_F = 0$. Moreover, via the gate voltage it is possible to tune the carrier density n according to the relation:

$$n = \varepsilon_d V_g / te \cong \alpha V_g \tag{17.3}$$

where ε_d is the dielectric permittivity of the gate dielectric, t is the gate thickness, and V_g is the gate voltage.

A direct consequence of relation (17.3) is the fact that the resistivity and conductivity depend strongly on the gate voltage. Using the Random Phase Approximation (RPA), the conductivity in graphene is given by [23]:

$$\sigma = \begin{cases} 20e^2 n^* / (hn_{imp}), & n - \bar{n} < n^* \\ 20e^2 n / (hn_{imp}), & n - \bar{n} > n^* \end{cases} \tag{17.4}$$

where h is the Planck constant and $\bar{n}$ and n^* are carrier concentrations determined via RPA Boltzmann theory. In the diffusive regime, we learn that charge transport is dominated by scattering from impurities with a concentration n_{imp} of the order of 10^{11} cm^{-2}. In the ballistic transport limit, at the Dirac point, the conductivity is $e^2/(\pi h)$.

Considering now the frequency dependence of the conductivity, it is a sum of frequency-dependent intraband and interband transitions in graphene, $\sigma_1(\omega)$ and $\sigma_2(\omega)$, respectively, as depicted in Fig. 17.3.

$$\sigma(\omega) = \sigma_1(\omega) + \sigma_2(\omega) \tag{17.5}$$

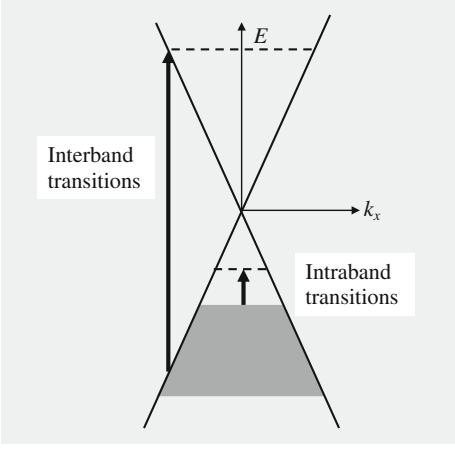

Fig. 17.3 The intraband and interband transitions in graphene

The intraband conductivity is given by:

$$\sigma_1(\omega) = ie^2 E_F/\pi\hbar^2(\omega + i/\tau) \tag{17.6}$$

while the interband term can be expressed as:

$$\sigma_2(\omega) = (ie^2\omega/\pi)\int_0^\infty [f(\varepsilon - E_F) - f(-\varepsilon - E_F)]/[(2\varepsilon)^2 - (\hbar\omega + i\Gamma)]d\varepsilon \tag{17.7}$$

where Γ is the momentum relaxation time, Γ is a broadening parameter and $f(E)$ is the Fermi-Dirac distribution function, which depends on the energy E of charge carriers. For $\tau = 40$ fs and small Fermi energy levels, of 100–200 meV, the intraband transitions and intraband conductivity is dominating up to 1 THz, the interband contributions being rather small or negligible. Beyond 100 THz, and up to the visible spectrum, only the interband transitions are relevant. For $\omega \to \infty$, the optical conductivity attains $e^2/4\hbar$, which leads to 2.3 % absorption in graphene at normal incidence, independent of the wavelength of the electromagnetic radiation. From the formulas (17.6) and (17.7), it can be seen that both intraband and interband conductivities depend on the Fermi energy, and so they can be changed by a gate voltage.

The single-wall CNT is a graphene sheet rolled-up around a chiral vector $\mathbf{C} = n\boldsymbol{a}_1 + m\boldsymbol{a}_2$ with n, m integers, which links two equivalent crystallographic sites. As a result, we have a confinement of carriers in the circumferential direction of the tube, given by the quantization rule:

$$\boldsymbol{k}_c\boldsymbol{C} = 2\pi j, \tag{17.8}$$

where $\boldsymbol{k}_c$ is the circumferential component of the wave vector $\boldsymbol{k}$ and $j = 1, 2, 3, \ldots, N$ is an integer. The quantization rule dictates that the allowed energy band structure of the CNT is obtained by cutting the 2D band of graphene into 1D slices. In the vicinity of a K point, for $ka \ll 1$, with $k = |\boldsymbol{k}|$ measured from K, the dispersion relation is linearly dependent on the wave vector k:

$$\omega(k) \cong 3^{1/2}ka/2 + \cdots \tag{17.9}$$

The CNT energy dependence on the wave vector can be expressed as

$$E_{\mathrm{CNT},j} = E_{2\mathrm{D}}(k\boldsymbol{K}_a/|\boldsymbol{K}_a| + j\boldsymbol{K}_c). \tag{17.10}$$

where $\boldsymbol{K}_c$ is a unit vector along the circumferential direction and $\boldsymbol{K}_a$ is the reciprocal lattice vector along the axis of the tube. The wave number k takes values in the interval $(-\pi/T, \pi/T)$, where T is the length of the translational vector $\boldsymbol{T}$. The above relation means that we have N discrete values of the CNT wave vector in the $\boldsymbol{K}_c$ direction, while in the $\boldsymbol{K}_a$ direction the wave vector is continuous. Thus, N lines of

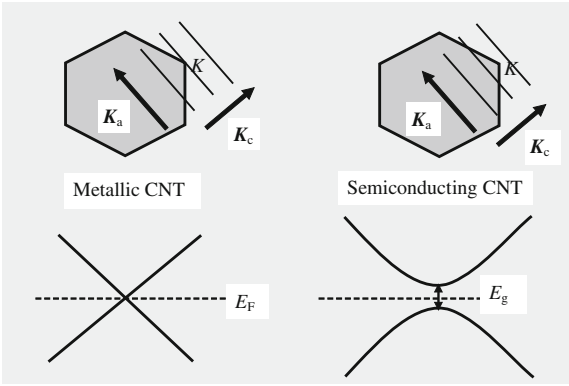

Fig. 17.4 CNT band structure

the form $k\boldsymbol{K}_a/|\boldsymbol{K}_a| + j\boldsymbol{K}_c$ cut the hexagonal Brillouin zone of graphene. We see in Fig. 17.4 that the CNT is metallic-like if the lines cross through the K point, and semiconductor-like otherwise. The CNT is metallic when $n - m = 3i$ and semiconductor when $n - m \neq 3i$, with i an integer. Moreover, at low energies the band structure of a metallic CNT consists of two bands with linear dispersion that intersect at the K point, while for semiconductor CNTs an energy gap E_g opens between the two bands.

The bandgap of the semiconducting CNT is given by:

$$E_g = 4\hbar v_F/3d, \tag{17.11}$$

and takes the value

$$E_g(\text{eV}) \cong 0.9/d(\text{nm}) \tag{17.12}$$

for the Fermi velocity $v_F = 8 \times 10^7$ m/s. Since semiconducting CNTs have diameters of at most few nanometers, their bandgap is in the range 20 meV–2 eV at room temperature.

17.2 Graphene Antennas at THz Frequencies

The graphene antennas are studied because they are able to provide to an antenna tunability and miniaturization. The first THz graphene antenna was reported in [24], where the fact that graphene is a tunable resistance, i.e. its resistance $R(V_g = 0\ \text{V})$ is of the order of 1 kΩ and decreases at tens of ohms for $R(V_g \gg 0\ \text{V})$ or $R(V_g \ll 0\ \text{V})$, was exploited to change the radiation pattern of a dipole or an array of dipoles.

As we have pointed out, in the range 1–30 THz the dominating term of conductivity is the interband conductivity, written in a simpler way as:

$$\sigma_{\text{inter}} = -i(e^2/4\pi\hbar)\ln\left(\frac{2|\mu_c| - \hbar(\omega - i2\Gamma)}{2|\mu_c| + \hbar(\omega - 2i\Gamma)}\right) \tag{17.13}$$

where μ_c is the chemical potential. In principle, the real part of the interband conductivity is much smaller than its imaginary part. On the other hand, both types of conductivity, i.e. interband and intraband, are taken into account in calculating the surface impedance in the THz range, despite the fact that interband conductivity is dominating. We have thus

$$Z_S(V_b) = 1/\sigma(\omega) = R_s(V_b) + jX_s(V_b). \tag{17.14}$$

The simulation data have shown [25] that the surface impedance is primarily reactive (inductive), R_s taking values below 52 Ω, whereas $X_s \gg R_s$ reaches 17–18 kΩ. This result implies that graphene is a high reactive impedance surface (RIS) having certain advantages:

(i) it reduces the lateral lobes
(ii) it enhances the front-to-back ratio of radiated power,
(iii) it minimizes the coupling between the antenna and its image, and assures antenna miniaturization [26].

Moreover, since both conductivity components depend on a gated DC electric field, the surface impedance can be modified by changing this field, graphene being a natural tunable high RIS.

As an example, we consider a gold THz dipole antenna with the length $L = 0.38$ $\lambda_0 = 11.25$ μm, the width $W = 1$ μm, a gap of 100 nm and a thickness of 200 nm deposited over a graphene monolayer, which on its turn is transferred onto Si/SiO_2, the SiO_2 having a thickness of 300 nm. The real and imaginary parts of the input impedance of the THz dipole on graphene are displayed in Fig. 17.5. There are many points where $X_s = 0$ or nearly zero.

The radiation pattern at 10 THz was simulated with the CST software, and is represented in Fig. 17.6. The radiation pattern shows no side lobes. The directivity of the antenna is of 6 dBi and its total efficiency is almost 15 %.

We have also analyzed a bow tie antenna with length $L = 0.38$ $\lambda_0 = 11.25$ μm, width $W = 1$ μm, and a gap of 100 nm made from gold with a thickness of 200 nm deposited onto graphene on Si/SiO_2. The radiation pattern at 10 THz, represented in Fig. 17.7, shows that the radiation efficiency is 33 % and the directivity is of about 8 dBi. Although it is well known that the bow-tie antenna has two lobes, a single lobe with a high directivity, able to collimate alone the 10 THz radiation without any lens, is evidenced in Fig. 17.7 as a net result of the RIS effect.

The inductive nature of the conductivity (RIS effect) in the THz region implies that TM surface plasmon polariton waves (SPPs) are propagating in graphene at the interface with air [27]. Using graphene on glass, the dimensions of the patch antennas are much smaller than L/λ_0, which is 0.06 for a microstrip patch with a length of 17 μm and width of 10 μm. Thus, SPP, which are occurring in principle at

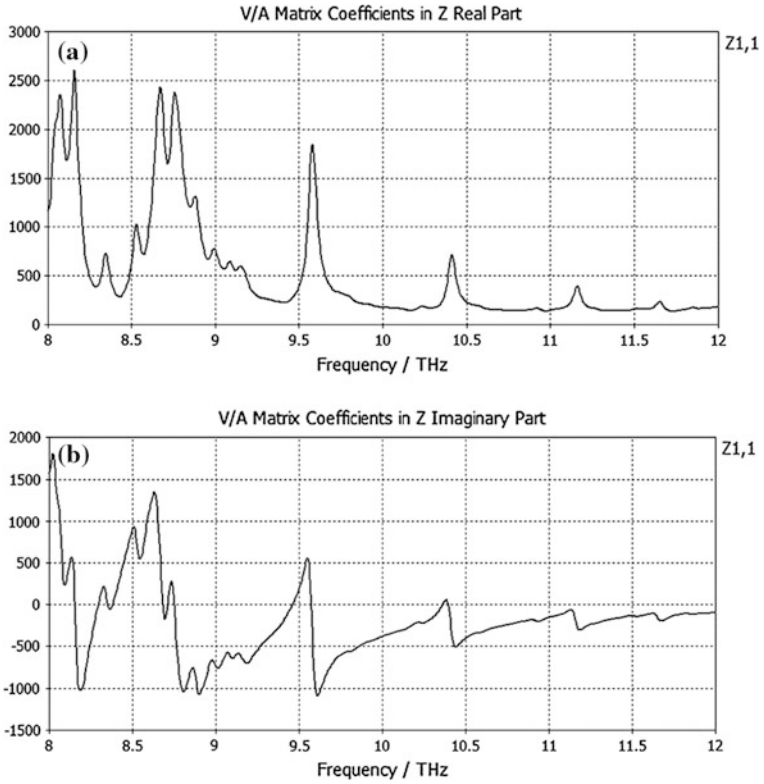

Fig. 17.5 The **a** real and **b** imaginary parts of the input impedance of a dipole on graphene at THz (after Dragoman et al. [25])

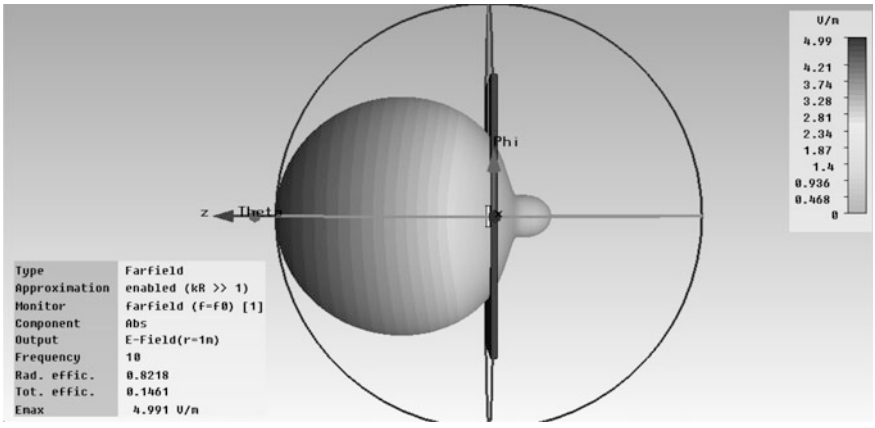

Fig. 17.6 The radiation pattern of a dipole on graphene at 10 THz (after Dragoman et al. [25])

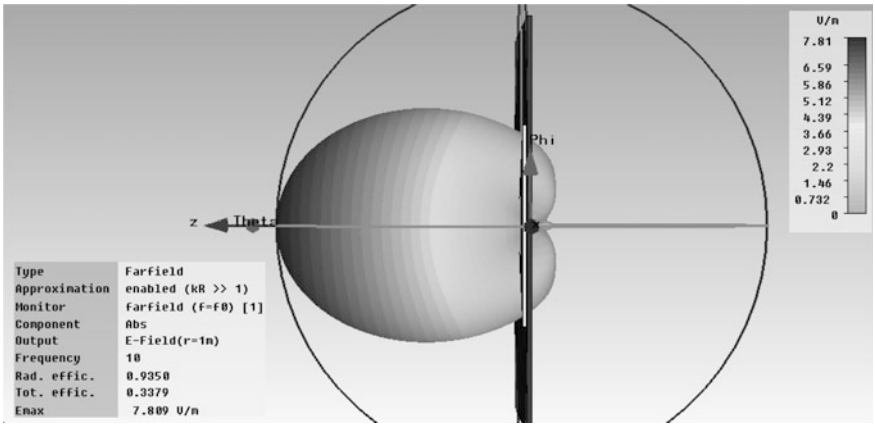

Fig. 17.7 The radiation pattern of a bow tie on graphene at 10 THz (after Dragoman et al. [25])

optical frequencies at metal/dielectric interfaces, are produced at much lower frequencies due to the unique physical properties of graphene. Moreover, the SPP waves in graphene are tunable and display stronger electromagnetic confinement and lower dissipation losses compared to SPP waves in metallic structures.

The SPP graphene antennas are resonant antennas working at the SPP resonance frequency [28] which is given by:

$$M\lambda/2n_{eff} = L + 2\delta L \tag{17.15}$$

where δL is the field penetration outside graphene and the effective index of refraction is:

$$n_{eff} = [1 - 4\mu_0/\varepsilon_0\sigma(\omega)] \tag{17.16}$$

with ε_0 and μ_0 the electric permittivity and magnetic permeability of the vacuum. The dispersion relation of SPPs propagating at the interface between two media with relative electric permittivities ε_{r1} and ε_{r2} can be written as:

$$\varepsilon_{r1}/(k^2 - \varepsilon_{r1}k_0^2)^{1/2} + \varepsilon_{r2}/(k^2 - \varepsilon_{r2}k_0^2)^{1/2} = -i\sigma/\omega\varepsilon_0 \tag{17.17}$$

where $k_0 = \omega/c$. Graphene rings structures are efficient plasmonic antennas at THz frequencies [29]. In this context, the wavenumber and resonant frequency of SPPs in graphene are given, respectively, by:

$$k_{SPP} \approx \hbar\omega^2/(2\alpha E_F c), \tag{17.18}$$

$$\omega_{SPP=}(nE_F/R). \tag{17.19}$$

It can be seen that the main parameters of the SPP wave, i.e. its wavenumber and resonance frequency, depend on the Fermi level, which can be tuned by a gate voltage. Therefore, SPP waves in graphene are tunable.

Emission of electromagnetic radiation via SPP is observed in graphene at impressive high frequencies, of 10^3 THz, and is generated at atomic scale by a point defect leading to SPP resonance at a sub-nanometer scale of about $\lambda/200$. The point defect is generated by replacing two carbon atoms with one Si atom representing a dopant atom, and an additional N atom bonded with the Si atom [30].

17.3 THz Generation Based on Graphene

THz generation using graphene is still in infancy, although some basic experiments have been reported. Most of them are based on the ultrafast excitation using a fs laser and various nonlinear effects in graphene. For instance, suspended graphene in a stripline configuration (see Fig. 17.8) was excited by a fs laser and photocurrents with a duration of maximum 4 ps were produced, corresponding to a spectrum up to 1 THz. The THz radiation is detected by the striplines electrodes, which act as a near-field antenna and as a waveguide up to 1 THz. The stripline has a length of 48 mm. The THz fields are due to build-in fields and a photothermoelectric effect. The THz radiation is collected by a field probe located at 0.3 mm away from graphene. In the graphene-based device, graphene was transferred on a low-temperature (LT) GaAs substrate, such that it spans the two striplines [31]. The graphene was illuminated by a titan-saphire laser with pulse duration of 160 fs and photon energy of 1.59 eV. The entire experimental configuration is a pump-probe set-up with a variable delay stage.

A further development of this approach based on graphene photoconductive switches is a chip containing graphene photoconductive switches for both generation and detection of ps pulses within THz range [31].

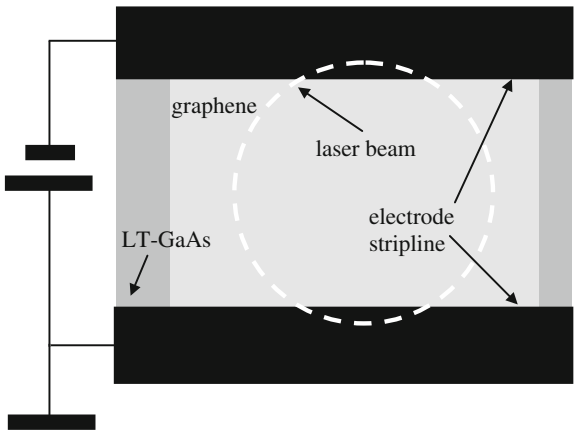

Fig. 17.8 THz generation via suspended graphene using biased striplines

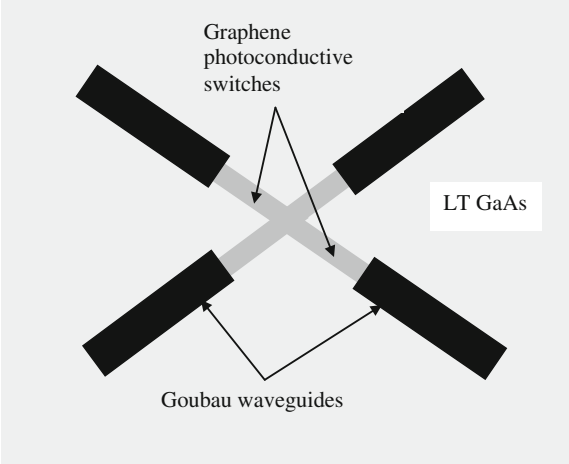

Fig. 17.9 THz generation/detection on chip with photoconductive switches

The photogeneration of charge carriers via visible light absorption encompasses several physical effects in time: (i) ultrafast phenomena are represented by carrier-carrier interactions (10 fs) resulting finally in a Fermi-Dirac distribution function followed by optical phonon scattering at 100 fs time scale with the net result of reducing the energy of hot carriers, (ii) slow phenomena at nanosecond time scale as a result of scattering between electrons and acoustic phonons due to the collisions between hot electrons and the crystalline lattice. None of these processes change the concentration of charge carriers, but both are inefficient, the dominant scattering mechanism being the collision between charge carriers and impurities.

The generation and detection of THz signals comprises several steps: (i) the photoconductive switch is illuminated by a fs laser, (ii) the THz signal is confined within a metal waveguide, and (iii) the interaction between the THz signal and crystalline materials results in absorption at certain resonant frequencies sensed by the second photoconductive switch. The transmitting and the receiving graphene switches are integrated on the same substrate with two planar Goubau waveguides, as depicted in Fig. 17.9.

Another method to generate THz signals is to use the strong nonlinear response in graphene. Third- and second-order optical nonlinearities were used for this aim. Second-order nonlinearities, encompassing difference-frequency and rectification processes, are stronger, but forbidden due to the centrosymmetry of graphene. Thus, an asymmetry is needed to use these strong nonlinearities and this asymmetry is introduced by photoexcitation with femtosecond laser pulses, and linked to in-plane photon wavenumbers. For example, a tilted incidence (e.g. at angles in the $\square = 20°–25°$ range) at the energy $\hbar\omega \gg 2E_F$ introduces the demanded anisotropy.

As it shown in Fig. 17.10 [32], THz generation is produced by the photon drag effect, which implies transfer of light momentum to photogenerated carriers in

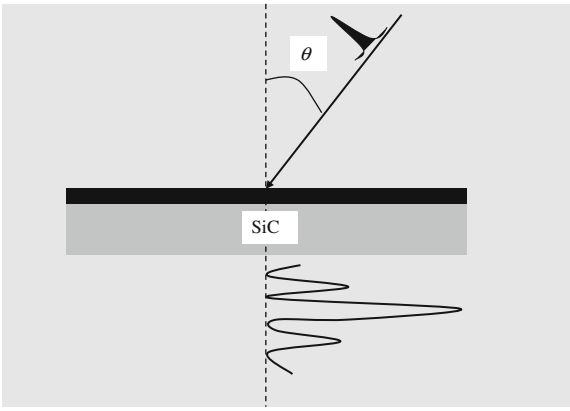

Fig. 17.10 The generation of THz pulses using second-order nonlinearities and the photon drag effect

multilayer graphene. The THz pulse is further transmitted through the SiC substrate and detected via electro-optic sampling.

Presently, THz lasers are designed and first experiments are undertaken to demonstrate that graphene is an amplifier medium for THz frequencies, with a maximum gain achieved so far of 8 cm^{-1} at 4 THz [33].

17.4 THz Detection Based on Graphene and Carbon Nanotubes

THz fields can be detected using graphene FETs with source and drain electrodes in the shape of various metallic antennas. The first experimental demonstration was the detection of a 0.3 THz signal at room temperature using a log-periodic circular-toothed antenna having the source electrode grounded and an outer radius of 322 μm. The channel length of the transistor was 10 μm. The detected signal at the drain contact is given by [34]:

$$\Delta V = (V_a^2/4)[1/\sigma(V_0)][d\sigma(V_g)/dV_g]\big|_{V_g=V_0} \tag{17.20}$$

where the gate voltage is written as $V_g(x,t) = V_0 + V_a \exp(-kx)\cos(\omega t - kx)$.

A bow-tie antenna was further used in the same configuration, i.e. a FET with a graphene channel and with source and drain electrodes in the shape of a bow-tie antenna. This time the channel length was 2.5 μm and the gate width was 2 μm. The THz signals were detected at 0.6 GHz with a noise-equivalent-power (NEP) of 500 $pW/Hz^{1/2}$ and a responsivity of 14 V/W [35]. In Fig. 17.11, we have schematically represented the bow-tie FET THz detector.

A simple logarithmic-periodic antenna, which has in the gap an interdigitated electrode consisting of 4 electrode pairs deposited over a graphene flake, is able also to detect THz radiation pulses (see Fig. 17.12). The THz detector has a rise time of

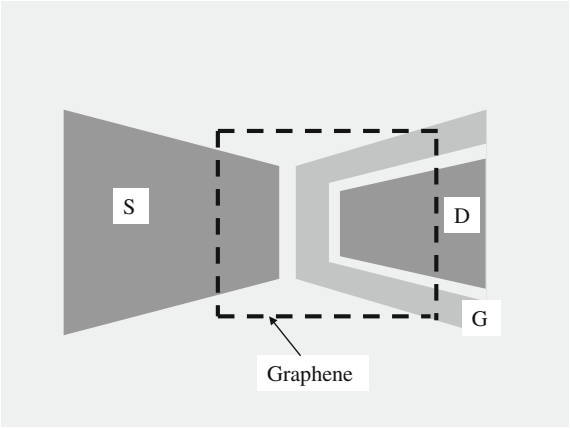

Fig. 17.11 Bow-tie antenna electrodes of a graphene FET for THz radiation

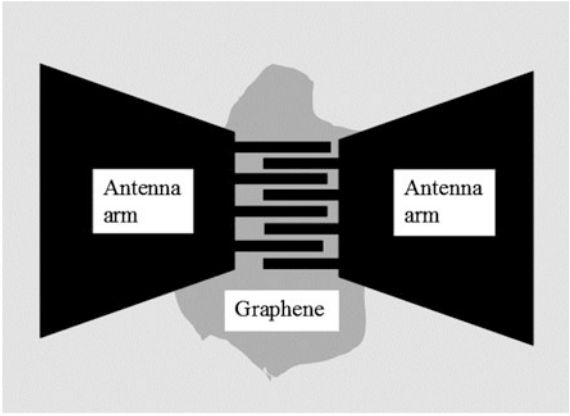

Fig. 17.12 Another graphene-based THz pulse detector

50 fs and is very simple, allowing the study of pulse shapes at the picosecond time scale [36].

Sensitive THz detection was demonstrated recently at room temperature with the help of the photothermoelectric effect in graphene [37]. The graphene has a significant interband absorption at THz. The carrier heat capacity in graphene is considerably reduced compared to bulk materials, implying that a larger temperature gradient is obtained for the same absorbed energy. This photothermoelectric effect has a picosecond time response and can be used for THz detection. Moreover, THz detection at room temperature is possible because the photothermoelectric effect is almost insensitive to temperature.

In experiments, two dissimilar metals distanced at 3 μm are used as electrodes for a graphene monolayer flake (see Fig. 17.13). The dissimilar metals consisting of overlapping regions of Cr and Au are obtained via consecutive and different angle evaporations of these metals. The carriers are heated by the incoming THz radiation, so that, if we consider the contacts as heat sinks, there is a temperature

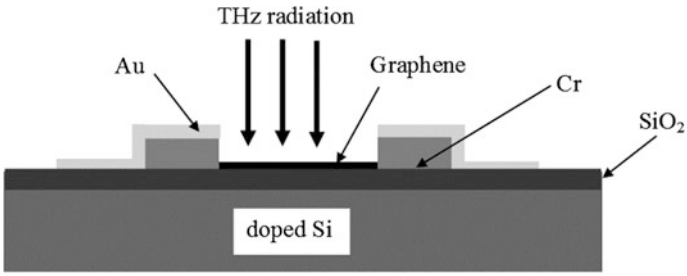

Fig. 17.13 Photothermoelectric THz detection

distribution $T(x)$ along the device. The diffusion of charge carriers produces a potential gradient

$$\nabla V(x) = -S\nabla T(x), \tag{17.21}$$

where S is the Seebeck coefficient of graphene, which is tunable by the backgate voltage and has a very large value [38]. The photodetector response is given by:

$$v = \int_0^L \nabla V(x)dx \tag{17.22}$$

This THz detector has a responsivity of 10 V/W (700 V/W) and a NEP of 1100 $pWHz^{-1/2}$ (20 $pWHz^{-1/2}$) when referring to the incident (absorbed) power.

A review of carbon nanotubes in THz was recently published [39], and the issues reported in this review will not be once again reviewed here. We note, however, that arrays of parallel CNTs were shown recently to behave as THz detectors with a responsivity of 2.5 V/W [40], and to produce THz radiation via optical excitations [41].

17.5 Conclusions

The results obtained in the last few years regarding THz devices based on carbon nanomaterials, and especially graphene, tell us that the famous THz gap will be closed soon by the further development of research in this 2D material. In particular, it is possible that THz graphene transistors that will be developed in few years based on room temperature ballistic transport in graphene will act as THz generators and mixers [42].

References

1. S. Iijima, Helical microtubules of graphitic carbon. Nature **354**, 56–58 (1991)
2. A.K. Geim, Graphene: status and prospects. Science **324**, 1530–1534 (2009)
3. D. Dragoman, M. Dragoman, Transport properties in carbon nanotube and graphene, in *Carbon Nanotubes and Graphene*, ed. by K. Tanaka, S. Iijima (Elsevier, Amsterdam 2014), pp. 151–165
4. F. Xia, H. Wang, D. Xiao, M. Dubey, A. Ramasubramaniam, Two-dimensional material nanophotonics. Nat. Photon. **8**, 899–907 (2014)
5. K.S. Novoselov, A.K. Geim, S.V. Morozov, D. Jiang, Y. Zhang, S.V. Dubonos, I.V. Grigorieva, A.A. Firsov, Electric field effect in atomically thin carbon films. Science **306**, 666–669 (2004)
6. A. Zurutuza, C. Marinelli, Challenges and opportunities in graphene commercialization. Nat. Nanotechnol. **9**, 730–734 (2014)
7. A.K. Geim, nobel lecture: random walk to graphene. Rev. Mod. Phys. **83**, 851–862 (2011)
8. A.V. Butenko, Dm. Shvarts, V. Sandomirsky, Y. Schlesinger, R. Rosenbaum, Hall constant in quantum-sized semimetal Bi films: Electric field effect influence. J. Appl. Phys. **88**, 2634–2640 (2000)
9. C.H. Ahn, A. Bhattacharya, M. Di Ventra, J.N. Eckstein, C.D. Frisbie, M.E. Gershenson, A. M. Goldman, I.H. Inoue, J. Mannhart, A.J. Millis, A.F. Morpurgo, D. Natelson, J.-M. Triscone, Electrostatic modification of novel materialsRev. Mod. Phys. **78**, 1185–1212 (2006)
10. M. Dragoman, G. Konstantinidis, K. Tsagaraki, T. Kostopoulos, D. Dragoman, D. Neculoiu, Graphene-like metal-on-silicon field-effect transistor. Nanotechnology **23**, 305201 (2012)
11. J. Renteria, R. Samnakay, C. Jiang, T.R. Pope, P. Goli, Z. Yan, D. Wickramaratne, T.T. Salguero, A.G. Khitun, R.K. Lake, A.A. Balandin, All-metallic electrically gated 2H-$TaSe_2$ thin-film and logic circuits. J. Appl. Phys. **115**, 034305 (2014)
12. S.P. Koenig, R.A. Doganov, H. Schmidt, A.H. Castro Neto, B. Özyilmaz, Electric field effect in ultrathin black phosphorus. Appl. Phys. Lett. **104**, 103106 (2014)
13. P.A. Merolla, J.V. Arthur, R. Alvarez-Icaza, A.S. Cassidy, J. Sawada, F. Akopyan, B.L. Jackson, N. Imam, C. Guo, Y. Nakamura, B. Brezzo, I. Vo, S.K. Esser, R. Appuswamy, B. Taba, A. Amir, M.D. Flickner, W.P. Risk, R.M.D.S. Modha, A million spiking-neuron integrated circuit with a scalable communication network and interface. Science **345,** 668–673 (2014)
14. S.-J. Han, A. Valdes Garcia, S. Oida, K.A. Jenkins, W. Haensch, Graphene radio frequency receiver integrated circuits. Nat. Comm. **3086** (2014)
15. A. Eatemadi, H. Daraee, H. Karimkhanloo, M. Kouhi, N. Zarghami, A. Akbarzadeh, M. Abasi, Y. Hanifehpourand, S.W. Joo, Carbon nanotubes: properties, synthesis, purification, and medical applications. Nano Res. Lett. **9**, 2–13 (2014)
16. M. Dragoman, D. Dragoman, *Nanoelectronics: Principles and Devices*, 2nd edn. (Artech House, Boston, 2009)
17. D. Dragoman, M. Dragoman, *Bionanoelectronics* (Springer, Heidelberg, 2012)
18. Y. Che, H. Chen, H. Gui, J. Liu, B. Liu, C. Zhou, Review of carbon nanotube nanoelectronics and macroelectronics. Semicond. Sci. Technol. **29**, 073001 (2014)
19. M.M. Shulaker, G. Hills, N. Patil, H. Wei, H.-Y. Chen, H.-S.P. Wong, S. Mitra, Carbon nanotube computer. Nature **501**, 526–530 (2013)
20. S. Chuang, Q. Gao, R. Kapadia, A.C. Ford, J. Guo, A. Javey, Ballistic InAs nanowire transistors. Nano Lett. **12**, 555–558 (2012)
21. A.M. Gilbertson, A. Kormanyos, P.D. Buckle, M. Fearn, T. Ashley, C.J. Lambert, S.A. Solin, L.F. Cohen, Room temperature ballistic transport in InSb quantum well nanodevices. Appl. Phys. Lett. **99**, 242101 (2011)
22. C. Neto, A.H.F. Guinea, N.M.R. Peres, K.S. Novoselov, A.K. Geim, The electronic properties of graphene. Rev. Mod. Phys. **81**, 109–162 (2009)

23. S. Adam, E.H. Hwang, V.M. Galitski, S. Das Sharma, A self-consistent theory of graphene transport, PNAS **104**, 18392–18395 (2007)
24. M. Dragoman, A.A. Muller, D. Dragoman, F. Coccetti, R. Plana, Terahertz antenna based on graphene. J. Appl. Phys. **107**, 104313 (2010)
25. M. Dragoman, M. Aldrigo, A. Dinescu, D. Dragoman, A. Costanzo, Towards a terahertz direct receiver based on graphene up to 10 THz. J. Appl. Phys. **115**, 044307 (2014)
26. H. Mosallaei, K. Sarabandi, Antenna miniaturization and bandwidth enhancement using a reactive impedance substrate. IEEE Trans. Antennas and Propag. **52**, 2403–2414 (2004)
27. M. Tamagnone, J.S.G. Diaz, J.R. Mosig, J. Perruisseau-Carrrier, Analysis and design of terahertz antennas based plasmonic resonant graphene sheets. J. Appl. Phys. **112**, 114915 (2012)
28. M. Dragoman, D. Dragoman, Plasmonics: applications to nanoscale terahertz and optical devices. Prog. Quant. Electron. **32**, 1–41 (2008)
29. P.W. Liu, W. Cai, L. Wang, X. Zhang, J. Xu, Tunablbe teraherz antennas based on graphene ring structures. Appl. Phys. Lett. **100**, 153111 (2012)
30. W. Zhou, J. Lee, J. Nanda, S.T. Pantelides, S.J. Pennycook, J.-C. Idrob, Atomically localized plasmon enhancement in monolayer graphene. Nat. Nanotechnol. **7**, 161–165 (2012)
31. N. Hunter, A.S. Mayorov, C.D. Wood, C. Russell, L. Li, E.H. Linfield, A.G. David, J.E. Cunningham, On-chip picosecond pulse detection and generation using graphene photoconductive switches. Nano Lett. **15**, 1591–1596 (2015)
32. J. Maysonnave, S. Huppert, F. Wang, S. Maero, C. Berger, W. van de Heer, T.B. Norris, L.A. de Vaulchier, S. Dhillon, J. Tignon, R. Ferreira, J. Mangeney, Terahertz generation by dynamical phonon drag effect in graphene excited by femtosecond optical pulses. Nano Lett. **14**, 5797–5802 (2014)
33. T. Otsuji, S.B. Tombet, A. Satou, M. Ryzhii, V. Ryzhii, Terahertz-wave generation using graphene: toward new types of terahertz lasers. IEEE J. Sel. Top. Quant. Electron. **19**, 8400209 (2013)
34. L. Vicarelli, M.S. Vitiello, D. Coquillat, A. Lombardo, A.C. Ferrari, W. Knap, M. Polini, V. Pellegrini, A. Tredicucci, Graphene field-effect transistors as room-temperature terahertz detectors. Nat. Mater. **11**, 865–871 (2012)
35. A. Zak, M.A. Andersson, M. Bauer, J. Matukas, A. Lisauskas, H.G. Roskos, J. Stake, Antenna-integrated 0.6 THz FET direct detectors based on CVD graphene. Nano Lett. **14**, 5834–5838 (2014)
36. M. Mittendorff, S. Winnerl, J. Kamann, J. Eroms, D. Weiss, H. Schneider, M. Helm, Ultrafast graphene-based broadband THz detector. Appl. Phys. Lett. **103**, 021113 (2013)
37. X. Cai, A.B. Sushkov, R.J. Suess, M.M. Jadidi, G.J. Jenkins, L.O. Nyakiti, R.L. Meyers-Ward, S. Li, J. Yan, D.K. Gaskill, T.E. Murphy, H.D. Drew, M.S. Fuhrer, Sensitive room-temperature terahertz detection via the photothermoelectric effect in graphene. Nat. Nanotechnol. **9**, 814–819 (2014)
38. D. Dragoman, M. Dragoman, Giant thermoelectric in graphene. Appl. Phys. Lett. **91**, 203116 (2007)
39. R.R. Hartmann, J. Kono, M.E. Portnoi, Terahertz science and btechnology of carbon nanomaterials. Nanotechnology **25**, 322001 (2014)
40. X. He, N. Fujimura, J.M. Lloyd, K.J. Erickson, A.A. Talin, Q. Zhang, W. Gao, Q. Jiang, Y. Kawano, R.H. Hauge, F. Leonard, J. Kono, Carbon nanotube terahertz detector. Nano Lett. **14**, 3953–3958 (2014)
41. L.V. Titova, C.L. Pint, Q. Zhang, R. Hauge, J. Kono, F.A. Hegmann, Generation of terahertz radiation by optical excitation of aligned carbon nanotubes, Nano Lett. **15** (2015) doi: 10.1021/acs.nanolett.5b00494
42. M. Dragoman, A. Dinescu, D. Dragoman, Negative differential resistance in graphene-based ballistic field-effect transistor with oblique top gate. Nanotechnology **25**, 415201 (2014)